A&A 671, A48 (2023)
https://doi.org/10.1051/0004-6361/202245598
© The Authors 2023

Astronomy & Astrophysics

Long-term optical variability of the Be/X-ray binary GRO J2058+42

P. Reig[1,2], A. Tzouvanou[2], D. Blinov[1,2], and V. Pantoulas[1]

[1] Foundation for Research and Technology - Hellas, 100 Nikolaou Plastira str., Vassilika Vouton, P.O. Box 1385, 70013 Heraklion, Crete, Greece
[2] University of Crete, Department of Physics, Voutes University Campus, 70013 Heraklion, Greece
e-mail: pau@physics.uoc.gr

Received 1 December 2022 / Accepted 17 January 2023

ABSTRACT

Context. GRO J2058+42 is a transient hard X-ray pulsar that occasionally goes into outburst. The optical counterpart is a poorly studied OB-type companion.
Aims. We investigate the long-term optical variability of the Be/X-ray binary GRO J2058+42 and the possible connection with periods of enhanced X-ray activity.
Methods. We performed an optical spectroscopic and photometric analysis on data collected during about 18 yr. We also present the first optical polarimetric observations of this source.
Results. The long-term optical light curves in the *BVRI* bands and the evolution of the Hα equivalent width display a sinusoidal pattern with maxima and minima that repeat every ∼9.5 yr. The amplitude of this variability increases as the wavelength increases from 0.3 mag in the *B* band to 0.7 in the *I* band. The Hα equivalent width varied from about −0.3 to −15 Å. We found a significant decrease in the polarization degree during the low optical state. The intrinsic polarization degree changed by ∼1% from maximum to minimum. The optical maxima occur near periods of enhanced X-ray activity and are followed by a drop in the optical emission. Unlike many other Be/X-ray binaries, GRO J2058+42 does not display *V*/*R* variability.
Conclusions. The long-term optical variability agrees with the standard model of a Be/X-ray binary, where the circumstellar disk of the Be star grows and dissipates on timescales of 9−10 yr. We find that the dissipation of the disk started after a major X-ray outburst. However, the stability of the Hα line shape as a double-peak profile and the lack of asymmetries suggest the absence of a warped disk and argue against the presence of a highly distorted disk during major X-ray outbursts.

Key words. stars: neutron – stars: emission-line, Be – X-rays: binaries

1. Introduction

GRO J2058+40 was discovered as a 198 s X-ray pulsar by BATSE on board the Compton Gamma-Ray Observatory (CGRO) during a giant outburst in 1995 September–October (Wilson et al. 1998). This giant (type II) outburst was followed by a series of weaker (type I) outbursts, whose intensity peaked at intervals of about 55 days (Wilson et al. 1998, 2005). Because BATSE detected the odd outbursts, counting from the giant outburst, to be brighter than even outbursts, it was proposed that GRO J2058+42 was undergoing periastron and apastron outburst in a 110 day orbit (Wilson et al. 1998). However, the all-sky monitor (ASM) on board the *Rossi* X-Ray Timing Explorer (RXTE) did not see such a pattern. Consequently, the orbital period was established to be 55 days (Wilson et al. 2005).

GRO J2058+42 was X-ray active from 1996 to 2002, but only detected at periastron passages. Pulsations were not detected during the epoch 2003−2004 (Wilson et al. 2005). GRO J2058+42 entered a new period of enhanced X-ray activity in May 2008 (Krimm et al. 2008). Although the X-ray flux doubled in less than a week, the luminosity was relatively low, $L_X = 1.5 \times 10^{36}$ erg s^{-1} assuming a distance of 9 kpc (Wilson et al. 2005; Reig & Fabregat 2015). This is more consistent with the lower-luminosity type I outbursts. However, because the 2008 X-ray data were limited to just one *Swift*/XRT pointed observation, it is likely that the peak of the outburst was missed.

Another giant X-ray outburst occurred in March 2019 with a peak luminosity in the energy range 3−78 keV of $L_X = 5.6 \times 10^{37}$ erg s^{-1} (Kabiraj & Paul 2020), similar to the discovery luminosity back in 1995. *NuSTAR* and AstroSat observations performed during this outburst revealed the possible presence of a cyclotron line at 10 keV together with some harmonics (Molkov et al. 2019; Mukerjee et al. 2020). During AstroSat observations, a quasi-periodic oscillation at 0.090 Hz was detected during the decay of the outburst (Mukerjee et al. 2020). The *NuSTAR* observations only detected the cyclotron line in a very narrow range of the spin phases of GRO J2058+42 and covering only ∼10% of the entire spin period (Molkov et al. 2019), but it did not seem to be present in the pulse-average spectrum (Kabiraj & Paul 2020).

The optical counterpart to GRO J2058+40 is an O9.5–B0e IV–V star (Reig et al. 2005; Wilson et al. 2005). The massive companion is a long-term variable system with photometric and spectroscopic changes on timescales of years (Kızıloğlu et al. 2007; Reig & Fabregat 2015; Reig et al. 2016). The underlying B star also displays fast optical multiperiodic variability that is attributed to nonradial pulsations (Kızıloğlu et al. 2007; Reig & Fabregat 2022). We present the most complete and detailed study of the optical variability of the BeXB GRO J2058+42 performed so far.

2. Observations and data analysis

We obtained optical photometry, spectroscopy, and polarimetry of the optical counterpart to GRO J2058+42. The observations

Open Access article, published by EDP Sciences, under the terms of the Creative Commons Attribution License (https://creativecommons.org/licenses/by/4.0), which permits unrestricted use, distribution, and reproduction in any medium, provided the original work is properly cited.
This article is published in open access under the Subscribe to Open model. Subscribe to A&A to support open access publication.

were made from the 1.3 m telescope at the Skinakas observatory[1] (SKO) in Crete (Greece). Additional spectra were retrieved from the data archive of the 2.0 m Liverpool Telescope[2] (LT).

2.1. Photometry

Photometric observations with the Johnson−Cousins B, V, R, and I filters were made with the 1.3 m telescope of the Skinakas Observatory. The telescope was equipped with a 2048×2048 ANDOR CCD with a 13.5 μm pixel size. In this configuration, the plate scale is 0.28″/pixel, hence providing a field of view of 9.5×9.5 arcmin^2. Standard stars from the Landolt list (Landolt 2009) were used for the transformation equations. The data were reduced in the standard way using the IRAF tools for aperture photometry[3] (Tody 1986). After the standardization process, we finally assigned an error to the calibrated magnitudes of the target given by the rms of the residuals between the cataloged and calculated magnitudes of the standard stars. The photometric magnitudes are given in Table A.1.

2.2. Polarimetry

Polarimetric observations were made with the RoboPol photopolarimeter attached to the focus of the 1.3 m telescope of the Skinakas Observatory. In the polarimetry configuration a plate scale of 0.43″/pixel is achieved with a 2048×2048 ANDOR CCD with a 13.5 μm pixel size. RoboPol is an imaging photopolarimeter that simultaneously measures the Stokes parameters of linear polarization of all sources in the field of view (King et al. 2014; Ramaprakash et al. 2019). RoboPol splits the incident light in two beams, each half incident on a half-wave retarder followed by a Wollaston prism. The fast axis of the half-wave retarder in front of the first prism is rotated by 67.5° with respect to the other retarder. Every point in the sky is thereby projected to four points on the CCD with different polarization state. The photon counts in each spot, measured using aperture photometry, were used to calculate the U and Q parameters of linear polarization. To optimize the instrument sensitivity, a mask was placed in the telescope focal plane. The absence of moving parts allows RoboPol to compute all the Stokes parameters of linear polarization in one shot. The intrumental polarization and polarization angle zero-point were controlled with regular measurements of polarimetric standards as described in Blinov et al. (2021). All observations were corrected for the instrumental polarization, and uncertainties were propagated accordingly. The results of the polarimetric observations are given in Table A.2.

2.3. Spectroscopy

The 1.3 m telescope at SKO was equipped with a 2048×2048 (13.5 micron) pixel ANDOR IKON CCD and a 1302 l mm^{-1} grating, giving a nominal dispersion of ∼0.9 Å/pixel. Spectra of comparison lamps were taken before and after each exposure in order to perform the wavelength calibration and account for small variations produced by the tension and flexture of the telescope at different zenith angles during the night that could affect the wavelength calibration The 2.0 m LT is a fully robotic telescope at the Roque de Los Muchachos on the Canary Island of La Palma (Spain). We downloaded and analyzed all the spectra available at the LT data archive for this source. These spectra were obtained with the Fibre-fed RObotic Dual-beam Optical Spectrograph (FRODOSpec), which is a dual-beam design multipurpose integral-field input spectrograph that splits the beam before the entrance to the individually optimized collimators. We used the spectra taken with the red arm, which cover the wavelength range 5900−8000 Å with a dispersion of 0.6 Å/pixel. A Xenon arc exposure was obtained after the science exposure. The log of the spectroscopic observations is given in Table A.4.

The Hα line is the prime indicator of the state of the disk. The structure and size of the disk affect not only the strength of the Hα line, but also its shape. We investigated the evolution of the strength and line profile over about an 18 yr period. We took the equivalent width of the Hα line (EW(Hα)) as a proxy of the strength of the line. To study the changes experienced by the shape of the line, we fit the line profile with one or two Lorentzian functions, depending on whether the line displayed a single-peak or a double-peak profile. In the case of a split profile, the peak at shorter wavelength is called the blue or violet peak, and it is denoted by V, and the peak at the longer wavelength is called the red peak and is represented by R.

The three fitting parameters are the central wavelength (λ_i), the full width at half maximum ($FWHM_i$), and the relative intensity of the peak (I_i). Here the subindex i refers to either the blue (V) or red peak (R). When the line showed a double-peak profile, we obtained the following quantities: $\Delta V = \lambda_R - \lambda_V$ and $V/R = \log(I_V/I_R)$, where I_V and I_R are the intensity of the blue and red peaks relative to the continuum. For single-peak profiles, $\Delta V = 0$ and $\log(V/R)$ was not defined.

The EW(Hα) was computed by means of a numerical integration method, the trapezoidal rule, as implemented in the scipy python package. To ensure an homogeneous processing, all the spectra were normalized with respect to the local continuum, which was rectified to unity by employing a polynomial fit. Because the definition of the continuum is the main source of uncertainty in the computation of the equivalent width, we averaged over different selections of the continuum and different polynomial fits (different grade). A total of 24 measurements were obtained for each spectrum. The error in EW(Hα) is the standard deviation of these measurements.

For the line fits, we used the `deblend` task of the SPLAT package (Škoda et al. 2014) of the Starklink project (Currie et al. 2014). The fits require the continuum to be at zero level. Therefore, the best polynomial fit of the continuum was subtracted from the spectra prior to the Lorentzian fits.

3. Results

3.1. Brightness variability

Figure 1 shows the long-term optical variability of GRO J2058+42. In general, the correlation among all optical observables is good. As the strength of the line emission increases, the continuum emission and the polarization increase. GRO J2058+42 went through two high and three low optical states during the course of our observations.

A closer look at Fig. 1 reveals some interesting results. First, the duration of the line emission in the low-optical states is significantly shorter than the continuum emission, that is, the changes in Hα occur on faster timescales than in the continuum. While the continuum emission may remain stable for years during the optical minimum, the Hα line emission reaches a minimum and begins to increase after just a few weeks. Second, the continuum emission reaches its peak by about ∼400 days before

[1] https://skinakas.physics.uoc.gr/en/
[2] https://telescope.livjm.ac.uk/
[3] A User's Guide to CCD Reductions with IRAF, Philip Massey, February 1997. https://iraf.net/irafdocs

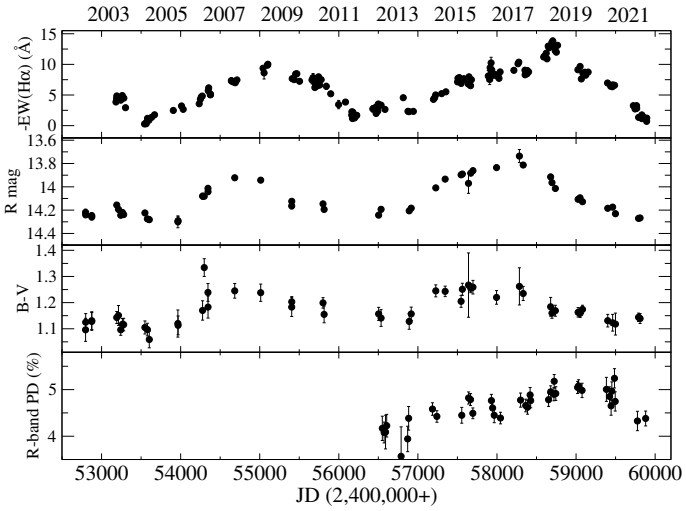

Fig. 1. Evolution of the optical observables. *From top to bottom*, we show the Hα equivalent width, continuum emission in the R band, $B-V$ color index, and polarization degree in the R band (not corrected for ISM polarization).

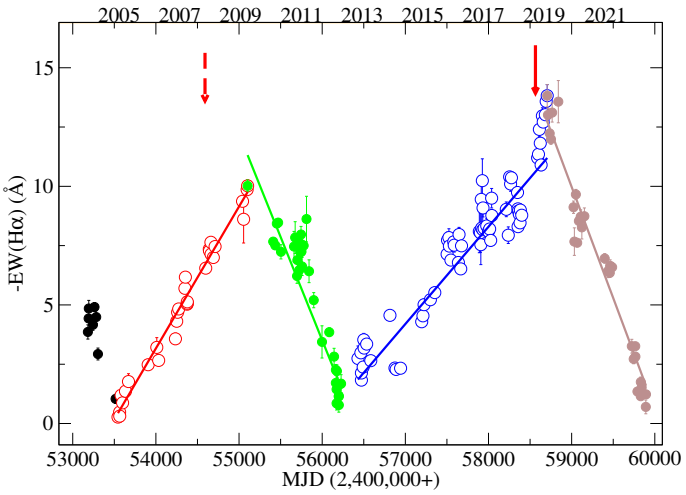

Fig. 2. Evolution of the Hα equivalent width. The circles represent the data, and the solid lines are the best linear fit to the data points of the corresponding interval. The red arrows mark the occurrence of an X-ray outburst. The dash style simply denotes a weaker outburst.

the EW(Hα) does. Third, the source exhibited stronger line and continuum emission during the 2019 high state than during the 2009 high state: EW(Hα) = −13.6 Å and R = 13.74 mag compared to EW(Hα) = −10 Å and R = 13.92 mag.

The transition from low to high states and then back to low states occurred smoothly over a period of several years. Overall, the rate of change in the EW(Hα) is roughly similar during the two transitions from the low to the high states as it is for the two declining phases. However, the changes in the optical observables during the declining phases are in general more abrupt that during the rising phases. To quantify this result, we performed a linear fit to the EW(Hα) for the four different phases, as shown in Fig. 2. The results are summarized in Table 1. The slopes of the fits are 1.5–2 times larger during the decay phase.

3.2. Hα line profile variability

In contrast to what it is typically seen in other BeXBs, the shape of the Hα line is rather symmetric. While the strength of the line changes substantially over time, as described in the previous section, the Be star in GRO J2058+42 always displays a quite symmetric double-peak profile (Fig. 3). The ratio of the peak intensities of the blue and red peaks is almost always $V/R \sim 1$ (Fig. 4, bottom panel), which it is rather unusual as most BeXBs exhibit V/R variability (Reig et al. 2000, 2010; Yan et al. 2016; Alfonso-Garzón et al. 2017; Zamanov et al. 2020).

The separation between the blue and red peaks ΔV also evolves with time and is anticorrelated with EW(Hα) (Fig. 4, top panel). At the optical high states, the peak separation approaches the spectral resolution of our data (∼200 km s^{-1}), and the two peaks merge into a single-peak profile in some spectra.

3.3. Optical polarimetry

The continuum polarization in Be stars is attributed to Thomson scattering of unpolarized starlight in the disk (Poeckert et al. 1979; Waters & Marlborough 1992; Wood et al. 1996; Yudin 2001; Halonen et al. 2013). In general, it is difficult to compute the actual intrinsic polarization because most of the observed polarization is expected to have an interstellar origin. For example, using the relation between polarization and extinction $P_{\rm max,ISM}$ (%) = 3.5 × $E(B-V)^{0.8}$ (Fosalba et al. 2002), we estimate that the maximum contribution of the interstellar medium (ISM) to the measured optical polarization toward GRO J2058+42 is $P_{\rm ISM}$ = 4.6%, which is the observed polarization, on average. However, the fact that the polarization degree varies by more than 1% (from ∼4% to ∼5.2%) and that this variation correlates with EW(Hα) (it increased as the EW(Hα) increased) supports the idea that part of the observed polarization is intrinsic to the source and originates in the disk. To estimate the contribution of the ISM, we observed three nearby stars in the field of view of GRO J2058+42. Table 2 lists the field stars that we used, while Table A.3 gives the polarimetric data for these stars.

Figure 5 shows the change in extinction with distance and the location of the field stars and the source. The data were taken from the dust maps by Green et al. (2019). The figure indicates that at least three different molecular clouds are in between the observer and the BeXB along the line of sight. Clearly, as the distance increases, so does the polarization. The field star fs2 is too close to Earth to represent a reliable measurement of the ISM polarization at the source distance. On the other hand, gfs2 displays stronger polarization than the source, which might indicate that the star is intrinsically polarized and hence again only a poor representation of the ISM polarization. We note that at very short and long distances, the computation of the extinction is very uncertain due to the lack of sufficient number of stars. If we use fs1 to estimate the polarization from the ISM (by vector subtraction, the Q and U Stokes parameters of the source and the field star), then we obtain that the intrinsic polarization varied from 0.3% to 1.3%. The lowest value of the polarization degree corresponds to the 2013 and 2022 observations, when the EW(Hα) displayed minimum values. The level of intrinsic polarization that we measure agrees with the expected polarization in an axisymmetric circumstellar disk predicted by single-scattering plus attenuation models, which is typically $\lesssim$2% (Waters & Marlborough 1992). It also agrees with the measured polarization in a sample of classical Be stars (Yudin 2001).

Table 1. Results of the linear fits to the different parts of the long-term evolution of the EW(Hα).

Region	MJD range	Slope	Ordinate	Corr. coef.	N_{obs}
Rise 1 (red)	53544–55103	0.00598 ± 0.00006	−320 ± 3	0.99	30
Rise 2 (blue)	56220–58751	0.00410 ± 0.00004	−230 ± 2	0.95	67
Decay 2 (green)	55103–56220	−0.00870 ± 0.00011	491 ± 6	−0.92	33
Decay 3 (brown)	58751–59894	−0.00938 ± 0.00010	560 ± 5	−0.98	31

Notes. See Fig. 2 to identify the various regions.

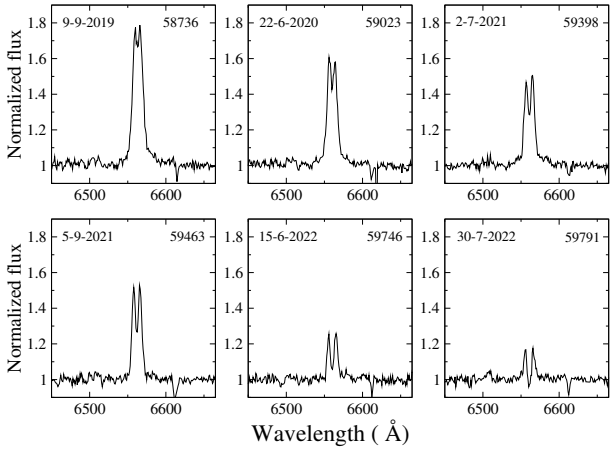

Fig. 3. Representative profiles of the Hα line.

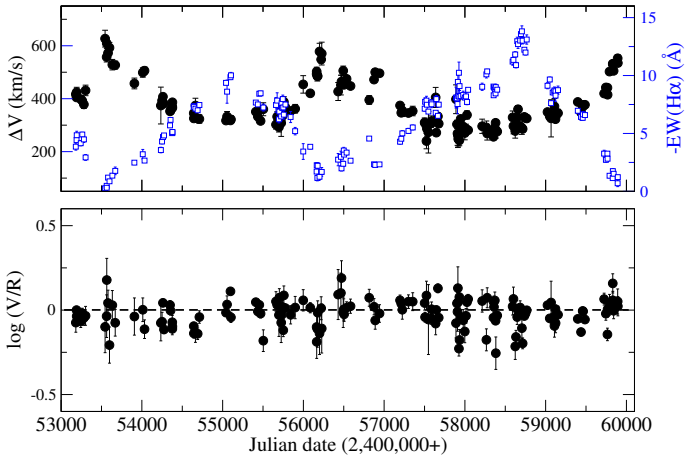

Fig. 4. Evolution of the Hα line parameters. *Top*: separation between the blue and red peaks (left axis) and the Hα EW (right axis). *Bottom*: evolution of the V/R ratio.

3.4. Reddening and distance

Owing to the presence of the circumstellar disk, the photometric magnitudes and colors are affected by disk emission. The overall effect is to make the star appear redder, that is, to be seen under higher extinction than in the absence of the disk. As a result, the estimate of the distance obtained from photometric magnitudes that are thought to be contaminated by disk emission represents a lower limit. Some attempts have been made to quantify the contribution of the disk to the photometric indices (Dachs et al. 1988; Fabregat & Reglero 1990; Riquelme et al. 2012). Here we take advantage of the low optical states in GRO J2058+42 (Fig. 1). Because the source of long-term optical variability is the disk, low optical states correspond to instances in which the disk is almost absent. Therefore, the low optical states give us the opportunity to observe the underlying B star without a major contribution from the disk.

Table 2. Selected field stars in the field of view of GRO J2058+42 used to derived the ISM polarization.

ID	RA	Dec	Distance (pc)	*Gaia* ID
fs1	314.72292	41.77444	1894^{+67}_{-48}	2065652877361883648
fs2	314.69167	41.76639	642^{+7}_{-6}	2065653598916381568
gfs2	314.77043	41.76491	5787^{+1771}_{-1095}	2065652671203453696

Notes. Distance from Bailer-Jones et al. (2021).

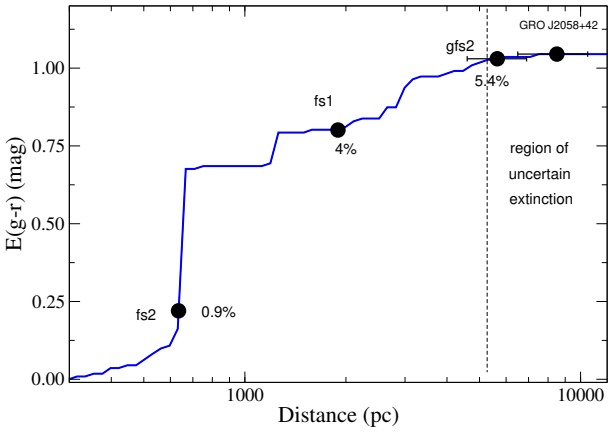

Fig. 5. Extinction as a function of distance (data from Green et al. 2019). The dots mark the assumed location of the stars on the extinction curve, according to their distance. Distances are from Bailer-Jones et al. (2021). We also indicate the polarization degree of each star (see Table A.3).

To estimate the distance through the distance-modulus relation, $V - M_V - A_V = 5\log(d) - 5$, the amount of interstellar extinction $A_V = R \times E(B-V)$ to the source has to be determined. The most direct method for estimating $E(B-V)$ is to use the calibrated color of the star according to the spectral type. The color excess is defined as $E(B-V) = (B-V)_{obs} - (B-V)_0$, where $(B-V)_{obs}$ is the observed color and $(B-V)_0$ is the intrinsic color of the star. The expected color for an O9.5–B0V star is $(B-V)_0 = -0.29 \pm 0.02$. This value is the average of the calibrations from Johnson (1966), Fitzgerald (1970), Gutierrez-Moreno (1979), Wegner (1994), and Pecaut & Mamajek (2013). The error is the standard deviation of the five values. We applied this method to the three low optical states independently and obtained 8.6 ± 0.9 kpc, 7.8 ± 0.8 kpc, and 8.0 ± 0.9 kpc for the 2005–2006, 2012–2013, and 2022–2023 low states. We note, however, that the average Hα EW was lowest during the 2005–2006

period at EW(Hα) = −0.9 Å, compared to EW(Hα) = −3.3 Å and EW(Hα) = −1.3 Å in the other two low states, respectively. Hence we take 8.5 ± 0.8 kpc as the final value for the distance. This value compares to $8.7^{+1.1}_{-0.9}$ kpc from *Gaia* (Bailer-Jones et al. 2021). The average color excess is estimated to be $E(B-V)$ = 1.42 ± 0.02.

4. Discussion

BeXBs display variability on all timescales and at all wavelengths. The fastest variability is detected in the X-rays (on the order of seconds) and corresponds to the rotation of the neutron star, which manifests as pulsations. In the optical band, the fastest timescales (on the order of hours or days) are attributed to changes in the stellar photosphere (pulsation and rotation). Long-term variations (on the order of months to years) are related to structural changes in the disk. These long-term variations are the subject of the present work.

4.1. Disk formation and dissipation

Be star disks are known to form and dissipate on timescales of years. The disk emission increases with wavelength and becomes particularly significant in the infrared band. GRO J2058+42 went through two high (2008–2009 and 2018–2019) and three low optical states (2004–2005, 2012–2013, and 2022–2023) during the course of our observations. The transition from low to high states and then back to low states occurred smoothly over a period of several years. We attribute these long-term changes to the formation and dissipation of the circumstellar disk. As expected in the disks of Be stars, the amplitude of the variability in the continuum increases as the effective wavelength increases: the difference in magnitudes from maximum to minimum is ΔB = 0.32, ΔV = 0.46, ΔR = 0.56, and ΔI = 0.70.

4.1.1. Line and continuum emission

In Sect. 3.1 we pointed out that the line emission variability timescales are faster than the continuum emission. The *BVRI* magnitudes can remain at a mean value with very small fluctuations during the low optical states. For example, in the period MJD 52800–54000, the mean and standard deviation of 14 measurements of the *V* magnitude were 14.94 and 0.04 mag, respectively. For MJD 55800–56900 (six measurements), these values were 14.90 and 0.02 mag, respectively. In contrast, EW(Hα) does not show a stable behavior like this and varies more strongly. For the same periods, the average and standard deviation in EW(Hα) was −1.8 and −0.8 Å and −2.7 and −2.1 Å, respectively.

Another interesting result is the fact that the peak in the EW(Hα) occurred about 400 days after the peak in the photometric magnitudes. Although the observational gaps cannot be ignored, the excellent spectral coverage clearly indicates that the delay between the EW(Hα) and *R*-band maxima is real. These delays imply that the continuum and line emission are anticorrelated for a certain period of time (i.e., the time elapsed between the two peaks). This result has been reported in many other BeXBs: Swift J0243.6+6124 (Liu et al. 2022), RX J0440.9+4431 (Yan et al. 2016), 1A 0535+26 (Clark et al. 1999; Yan et al. 2012), 4U 0115+63 (Reig et al. 2007), and SAX J2103.5+4545 (Camero et al. 2014). Interestingly, the X-ray outbursts occur close to the EW(Hα) maxima.

This delay can be explained as due to the different locations in the disk in which the line and continuum emission in Be stars originate. The outer parts of the disk contribute most to the emission of the Hα line, whereas the origin of the optical continuum resides in the inner parts. According to the viscous decretion disk model (see Rivinius et al. 2013, for a review), about 90−95% of the *V*-band flux comes from inside 1.8−2.5 R_* (Haubois et al. 2012), while Hα emission reaches this percentage above $\gtrsim$6−10 R_* (Carciofi 2011). Therefore, the fact that the optical brightness has already started to decrease by the time the EW(Hα) reached the maximum indicates that the dissipation of the disk began from the inner parts of the disk. Disk dissipation occurs when the mass ejection mechanism ceases. As the angular momentum supply stops, the inner parts of the disk are reaccreted onto the star. However, viscosity still transports angular momentum outward. Thus the outer parts of the disk continue to expand, while the inner parts move inward (Haubois et al. 2012; Carciofi et al. 2012). Since the flux in the *V* (or *R*) band is mainly produced in the inner parts of the disk, we expect the visual flux to start decreasing before the Hα line flux, which mainly originates in the outer parts.

The long-term trend of the polarization degree also supports a disk formation and dissipation cycle. Polarization in Be stars results from the scattering of stellar radiation by electrons in the circumstellar disk. The degree of the polarization provides information about the number of scatterers. Therefore, we should expect a significant decrease in the polarization degree during low optical states, as is indeed observed (Fig. 1). Since these low optical states represent instances when the disk almost vanished, we can assume that the polarization degree roughly corresponds with that of the ISM. With this assumption, we estimate that the ISM polarization from the observer to GRO J2058+42 is ∼4%.

Strictly speaking, none of the low optical states corresponded to the complete loss of the disk because the Hα line did not revert fully into absorption (see Fig. 3). A normal (i.e., non-Hα emitting) B0V star is expected to have EW(Hα) = +3.5 Å (Jaschek & Jaschek 1987), while the lowest values of EW(Hα) during the low optical states were around −[0.3 − 1] Å. Nevertheless, the low optical states do represent highly debilitated disk phases.

4.1.2. Connection with X-rays

As we mentioned above, the EW(Hα) during the 2018–2019 maximum reached higher values than during the 2008–2009 high state. Since EW(Hα) provides a measure of the size of the disk, we conclude that the Be star developed a larger disk during the 2018–2019 event. The accretion of a large amount of matter onto the neutron star led to the type II outburst observed by the *NuSTAR* and Astrosat space missions. In principle, it might be argued that since the disk was smaller during the 2008–2009 optical peak, the X-ray emission would be lower, as observed. On the other hand, given the similarities and regularity of the low and high optical states (Figs. 1 and 2), the absence of a giant X-ray outburst prior to the 2008–2009 optical maximum is surprising. The *Swift*/BAT hard X-ray transient monitor detected an increase in 15−50 keV flux by a factor of two in less than a week. A pointed observation with *Swift*/XRT was made on 9 May 2008. The 0.3−10 keV flux was estimated to be 1.5×10^{-10} erg cm^{-2} s^{-1}, which at a distance of 9 kpc corresponds to a luminosity of $L_X = 1.4\times10^{36}$ erg s^{-1} (Krimm et al. 2008). Although this luminosity is one order of magnitude lower than the 2019 event, we cannot be sure that it corresponded to the peak of the X-ray event. The 2008–2009 is reminiscent of

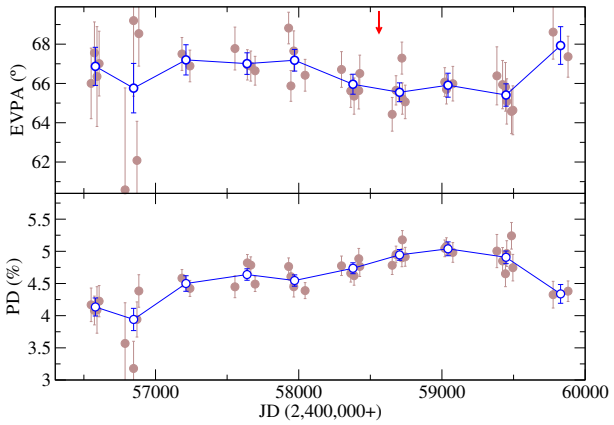

Fig. 6. Polarization angle and polarization degree of GRO J2058+42 for the period 2013–2022. The red arrow marks the occurrence of a type II outburst. Filled brown circles denote all the observations, and the open blue circles represent the weighted mean calculated using the observations over one year.

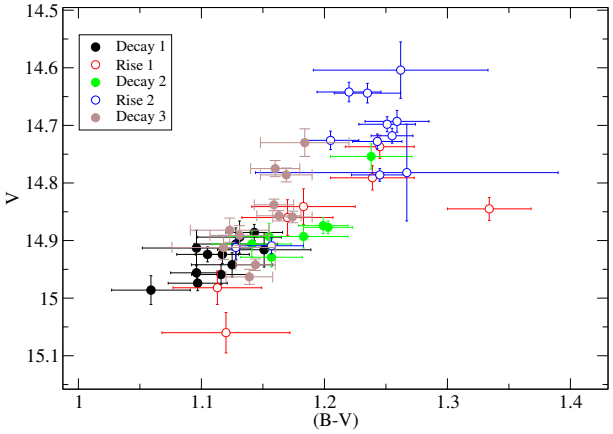

Fig. 7. $(B-V)-V$ color magnitude diagram. Empty symbols correspond to the disk formation phases, and filled symbols correspond to the dissipation phases.

a type I outburst, and the lack of data can be attributed to the weakness of the detection due to the large distance to the source.

One possible explanation for the different luminosity of the two events could be a different geometry in a misaligned and tilted disk. Current models that explain X-ray outbursts in BeXBs invoke warped, tilted, and misaligned disks. Because disks in BeXBs are truncated (Reig et al. 1997, 2016), the only way for large amount of material to be transferred to the neutron star is in highly asymmetric configurations in which a misaligned disk becomes warped and eccentric. Highly distorted disks result in enhanced mass accretion when the neutron star moves across the warped part (Martin et al. 2011, 2014; Okazaki et al. 2013). Evidence of these warped disks has been reported for 1A 0535+262 (Moritani et al. 2013) based on a spectral line analysis and for 4U 0115 (Reig & Blinov 2018) based on variations in the polarization angle. Although we observe a small change in the polarization angle during the 2019 X-ray outburst (Fig. 6), it is not very significant. Likewise, the symmetry of the Hα line profile argues against a highly distorted disk. Therefore, it remains to be seen how a type I outburst can lead to the almost complete destruction of the circumstellar disk.

We also noted in Sect. 3.1 that the dissipation of the disk is faster than its formation. The rate of change of the Hα equivalent width is about 1.8 Å yr^{-1} during disk formation and about 3.3 Å yr^{-1} during disk dissipation (see Fig. 2 and Table 1). This result contrasts with what it is observed in classical Be stars, in which the timescales for disk growth are shorter than the timescales for disk dissipation (Haubois et al. 2012). A crucial difference is the presence of the neutron star in BeXBs. As the disk expands and reaches periastron distance, a substantial amount of matter will be accreted onto the neutron star. Therefore, the dissipation of the disk in BeXBs may occur faster owing to the interaction between the neutron star and the disk.

4.2. Inclination angle

We showed in Sect. 3.2 that the source displays a double-peak profile even during the high optical state (see Fig. 3). This result suggests that we see the circumstellar disk at an intermediate inclination angle. Typically, single-peak profiles are associated with high inclination angles (pole-on stars) and shell profiles with high inclination angles (edge-on stars; Slettebak 1979; Hanuschik 1995; Rivinius et al. 2006; Silaj et al. 2014; Sigut & Ghafourian 2022). An example of a low inclination system is V 0332+54, whose inclination angle is estimated to be $i < 20°$ (Negueruela et al. 1999; Zhang et al. 2005), and a BeXB that exhibits shell profiles is IGR J21343+4738 (Reig & Zezas 2014).

The evolution of the photometric magnitudes and colors can also be used to constrain the inclination angle. Figure 7 shows the color-magnitude diagram of GRO J2058+42. Empty symbols correspond to the disk formation phases, and filled symbols correspond to the dissipation phases. The positive correlation between the color index $(B-V)$ and the V magnitude implies that the system is viewed at an intermediate inclination angle, where the disk emission to the optical colors and magnitudes contributes significantly. As the disk grows, the system brightens (V decreases), while the overall (disk plus star) emission becomes redder ($(B-V)$ increases). At very high inclination angles (equator-on stars), the inner parts of the Be envelope partly block the stellar photosphere, while the small projected area of the disk on the sky keeps the disk emission to a minimum. Thus, stars viewed at very high inclination angles ($i > i_{\rm crit}$) would show an inverse correlation (Harmanec 1983; Harmanec et al. 2000). The value of the critical inclination angle is not known, but a rough estimate based on available data suggests $i_{\rm crit} \sim 60{-}70°$ (Hanuschik 1996; Sigut & Patel 2013). In summary, the correlation between the photometric colors and magnitudes and the stable double peak profile of the Hα line in GRO J2058+42 suggest an inclination angle in the range 30°−60°.

4.3. Disk size and kinematics

It was already proposed by Struve (1931) that disks in Be stars are supported by rotation. The main evidence for this comes from the correlation between the projected rotational velocity and the width and shape of the emission line (Andrillat 1983; Dachs et al. 1986, 1992; Hanuschik et al. 1988; Hanuschik 1989).

In Sect. 3.2 we showed that the peak separation ΔV and EW(Hα) are anticorrelated. This is the expected behavior in rotation-supported disks, in which the rotational velocity of the gas particles in the disk varies as the inverse of the radius, $v_\phi \propto r^{-j}$ (e.g., for Keplerian disks $j = 1/2$). In these disks, the

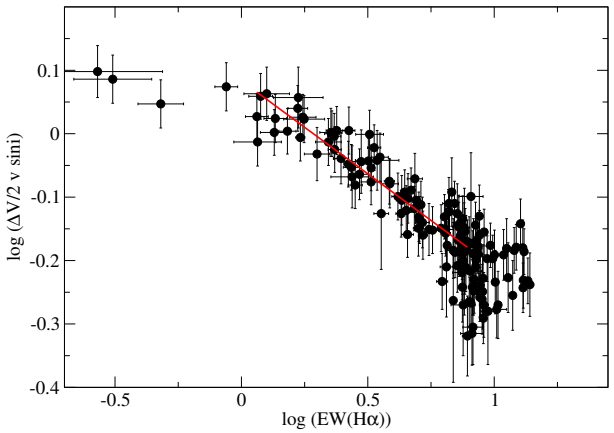

Fig. 8. Peak separation as a function of EW(Hα).

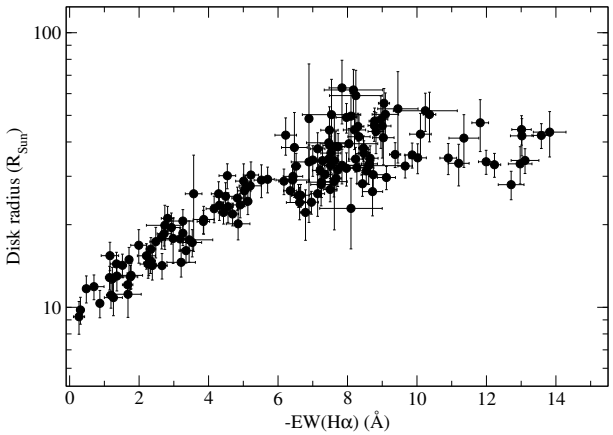

Fig. 9. Disk radius as a function of EW(Hα).

peak separation roughly corresponds to twice the projected rotational velocity of the particles in the disk $\Delta V \approx 2v_\phi \sin i$. As the radius of the disk increases (i.e., as EW(Hα) increases), the rotational velocity decreases, and so does the peak separation. The index j can be estimated from the relation between peak separation and EW (Hanuschik et al. 1988),

$$\log(\Delta V/2 \sin i) = a \times \log(\mathrm{EW}(\mathrm{H}\alpha)) + b, \quad (1)$$

where the slope a is related to the j index as $a = j/2$. Figure 8 shows this relation for GRO J2058+42. When we restrict the fitting range to EWs between 1 and 8 Å, then we find $j = 0.58 \pm 0.04$, which is not far from the expected value of 0.5 for a Keplerian disk. Lower and higher values of the EW(Hα) were removed from the fit because below $\log(\mathrm{EW}(H\alpha)) \sim 0$ the disk is too small and has probably not reached a stable configuration, while above 8 Å, the ΔV saturates, which might be a spectral resolution effect.

After showing that the particles in the disk of GRO J2058+42 follow a Keplerian law, we can estimate the disk size. The disk velocity adopts the form (see. e.g., Huang 1972)

$$v_\phi = v_0 \left(\frac{r}{R_*}\right)^{-1/2}, \quad (2)$$

where R_* is the equatorial stellar radius, and v_0 is a initial value of the disk velocity close to the stellar surface. In the limiting case, v_0 would be the stellar rotational velocity. For simplicity, we assumed $v_0 = v_*$. By inverting Eq. (2) and since $v_\phi \approx (\Delta V/2 \sin i)$,

$$\frac{R_\mathrm{d}}{R_*} = \left(\frac{2v_* \sin i}{\Delta V}\right)^2, \quad (3)$$

where $r = R_\mathrm{d}$ is the radius of the Hα emission region. Figure 9 shows the size of the circumstellar disk as a function of time and EW(Hα). As mentioned above, the leveling off at $\sim 50\,R_\odot$ marks the minimum distance between the peaks that our spectrograph is capable of discerning.

The Be star projected rotational velocity in GRO J2058+42 has been estimated by Kızıloğlu et al. (2007) to be in the range 240–310 km s^{-1}. Here we assumed $v_* \sin i = 275$ km s^{-1}, which corresponds to half the maximum peak separation. We note, however, that Hα double-peak separation exceeding $2v_* \sin i$ has been measured in Be stars during phases of very weak Hα emission (Dachs et al. 1992).

The largest disk radius is estimated to be $R_\mathrm{disk,max} \sim 5$–$6\,R_*$ or $60\,R_\odot$, assuming a stellar radius of an O9.5–B0e IV–V star of $10\,R_\odot$ (Martins et al. 2005). From Kepler's third law, we can estimate the orbital separation $a \sim 160\,R_\odot$ for $P_\mathrm{orb} = 55$ days and typical values of the mass $M_* = 18\,M_\odot$. If we now assume that in order to produce an X-ray outburst, the neutron star must interact with the disk, that is, the disk radius must be similar to the periastron distance ($a(1-e)$), then the eccentricity of the system should be $e \sim 0.6$.

5. Conclusion

We have performed the most detailed study of the long-term optical variability of the BeXB GRO J2058+42. The system displays correlated variability on timescales of years in all the optical observables. The source goes through optical high and low states. The high optical state is characterized by large EW(Hα), bright continuum emission, and significant polarization. We identify this state with a well-developed decretion disk. The smooth increases and decreases of the optical emission are interpreted as phases of formation and dissipation of the circumstellar disk. The optical maxima coincide with the occurrence of X-ray outbursts, after which all optical indicators decreased, leading to the dissipation of the disk. However, a disk-loss episode never occurred. The almost permanent double-peak line profile indicates that the systems is seen at an intermediate inclination angle, whereas the absence of V/R variability is attributed to a relatively small and stable disk. We did not find evidence for a warped disk during the 2019 type II X-ray outburst.

Acknowledgements. Skinakas Observatory is run by the University of Crete and the Foundation for Research and Technology-Hellas. The Liverpool Telescope is owned and operated by the Astrophysics Research Institute of Liverpool John Moores University. The Starlink software is currently supported by the East Asian Observatory. IRAF is distributed by the National Optical Astronomy Observatories, which is operated by the Association of Universities for Research in Astronomy, Inc. (AURA) under cooperative agreement with the National Science Foundation. This research has made use of the SIMBAD database, operated at CDS, Strasbourg, France and of NASA's Astrophysics Data System operated by the Smithsonian Astrophysical Observatory.

References

Alfonso-Garzón, J., Fabregat, J., Reig, P., et al. 2017, A&A, 607, A52
Andrillat, Y. 1983, A&AS, 53, 319
Bailer-Jones, C. A. L., Rybizki, J., Fouesneau, M., Demleitner, M., & Andrae, R. 2021, AJ, 161, 147
Blinov, D., Kiehlmann, S., Pavlidou, V., et al. 2021, MNRAS, 501, 3715
Camero, A., Zurita, C., Gutiérrez-Soto, J., et al. 2014, A&A, 568, A115

Carciofi, A. C. 2011, in IAU Symposium, eds. C. Neiner, G. Wade, G. Meynet, & G. Peters, 272, 325
Carciofi, A. C., Bjorkman, J. E., Otero, S. A., et al. 2012, ApJ, 744, L15
Clark, J. S., Lyuty, V. M., Zaitseva, G. V., et al. 1999, MNRAS, 302, 167
Currie, M. J., Berry, D. S., Jenness, T., et al. 2014, in Astronomical Data Analysis Software and Systems XXIII, ed. N. Manset, ASP Conf. Ser., 485, 391
Dachs, J., Hanuschik, R., Kaiser, D., & Rohe, D. 1986, A&A, 159, 276
Dachs, J., Kiehling, R., & Engels, D. 1988, A&A, 194, 167
Dachs, J., Hummel, W., & Hanuschik, R. W. 1992, A&AS, 95, 437
Fabregat, J., & Reglero, V. 1990, MNRAS, 247, 407
Fitzgerald, M. P. 1970, A&A, 4, 234
Fosalba, P., Lazarian, A., Prunet, S., & Tauber, J. A. 2002, ApJ, 564, 762
Green, G. M., Schlafly, E., Zucker, C., Speagle, J. S., & Finkbeiner, D. 2019, ApJ, 887, 93
Gutierrez-Moreno, A. 1979, PASP, 91, 299
Halonen, R. J., Mackay, F. E., & Jones, C. E. 2013, ApJS, 204, 11
Hanuschik, R. W. 1989, Ap&SS, 161, 61
Hanuschik, R. W. 1995, A&A, 295, 423
Hanuschik, R. W. 1996, A&A, 308, 170
Hanuschik, R. W., Kozok, J. R., & Kaiser, D. 1988, A&A, 189, 147
Harmanec, P. 1983, Hvar Obs. Bull., 7, 55
Harmanec, P. 2000, in IAU Colloq. 175: The Be Phenomenon in Early-Type Stars, eds. M. A. Smith, H. F. Henrichs, & J. Fabregat, ASP Conf. Ser., 214, 13
Haubois, X., Carciofi, A. C., Rivinius, T., Okazaki, A. T., & Bjorkman, J. E. 2012, ApJ, 756, 156
Huang, S.-S. 1972, ApJ, 171, 549
Jaschek, C., & Jaschek, M. 1987, The Classification of Stars (Cambridge: Cambridge University Press)
Johnson, H. L. 1966, ARA&A, 4, 193
Kabiraj, S., & Paul, B. 2020, MNRAS, 497, 1059
King, O. G., Blinov, D., Ramaprakash, A. N., et al. 2014, MNRAS, 442, 1706
Kızıloğlu, U., Kızıloğlu, N., Baykal, A., Yerli, S. K., & Özbey, M. 2007, A&A, 470,
Krimm, H. A., Barthelmy, S. D., Baumgartner, W., et al. 2008, ATel, 1516, 1
Landolt, A. U. 2009, AJ, 137, 4186
Liu, W., Yan, J., Reig, P., et al. 2022, A&A, 666, A110
Martin, R. G., Pringle, J. E., Tout, C. A., & Lubow, S. H. 2011, MNRAS, 416, 2827
Martin, R. G., Nixon, C., Armitage, P. J., Lubow, S. H., & Price, D. J. 2014, ApJ, 790, L34
Martins, F., Schaerer, D., & Hillier, D. J. 2005, A&A, 436, 1049
Molkov, S., Lutovinov, A., Tsygankov, S., Mereminskiy, I., & Mushtukov, A. 2019, ApJ, 883, L11
Moritani, Y., Nogami, D., Okazaki, A. T., et al. 2013, PASJ, 65, 83
Mukerjee, K., Antia, H. M., & Katoch, T. 2020, ApJ, 897, 73
Negueruela, I., Roche, P., Fabregat, J., & Coe, M. J. 1999, MNRAS, 307, 695
Okazaki, A. T., Hayasaki, K., & Moritani, Y. 2013, PASJ, 65, 41
Pecaut, M. J., & Mamajek, E. E. 2013, ApJS, 208, 9
Poeckert, R., Bastien, P., & Landstreet, J. D. 1979, AJ, 84, 812
Ramaprakash, A. N., Rajarshi, C. V., Das, H. K., et al. 2019, MNRAS, 485, 2355
Reig, P., & Blinov, D. 2018, A&A, 619, A19
Reig, P., & Fabregat, J. 2015, A&A, 574, A33
Reig, P., & Fabregat, J. 2022, A&A, 667, A18
Reig, P., & Zezas, A. 2014, A&A, 561, A137
Reig, P., Fabregat, J., & Coe, M. J. 1997, A&A, 322, 193
Reig, P., Negueruela, I., Coe, M. J., et al. 2000, MNRAS, 317, 205
Reig, P., Negueruela, I., Papamastorakis, G., Manousakis, A., & Kougentakis, T. 2005, A&A, 440, 637
Reig, P., Larionov, V., Negueruela, I., Arkharov, A. A., & Kudryavtseva, N. A. 2007, A&A, 462, 1081
Reig, P., Zezas, A., & Gkouvelis, L. 2010, A&A, 522, A107
Reig, P., Nersesian, A., Zezas, A., Gkouvelis, L., & Coe, M. J. 2016, A&A, 590, A122
Riquelme, M. S., Torrejón, J. M., & Negueruela, I. 2012, A&A, 539, A114
Rivinius, T., Štefl, S., & Baade, D. 2006, A&A, 459, 137
Rivinius, T., Carciofi, A. C., & Martayan, C. 2013, A&ARv, 21, 69
Sigut, T. A. A., & Ghafourian, N. R. 2022, arXiv e-prints [arXiv:2209.06885]
Sigut, T. A. A., & Patel, P. 2013, ApJ, 765, 41
Silaj, J., Jones, C. E., Sigut, T. A. A., & Tycner, C. 2014, ApJ, 795, 82
Škoda, P., Draper, P. W., Neves, M. C., Andrešič, D., & Jenness, T. 2014, Astron. Comput., 7, 108
Slettebak, A. 1979, Space Sci. Rev., 23, 541
Struve, O. 1931, ApJ, 73, 94
Tody, D. 1986, in Instrumentation in Astronomy VI, ed. D. L. Crawford, SPIE Conf. Ser., 627, 733
Waters, L. B. F. M., & Marlborough, J. M. 1992, A&A, 256, 195
Wegner, W. 1994, MNRAS, 270, 229
Wilson, C. A., Finger, M. H., Harmon, B. A., Chakrabarty, D., & Strohmayer, T. 1998, ApJ, 499, 820
Wilson, C. A., Weisskopf, M. C., Finger, M. H., et al. 2005, ApJ, 622, 1024
Wood, K., Bjorkman, J. E., Whitney, B. A., & Code, A. D. 1996, ApJ, 461, 828
Yan, J., Li, H., & Liu, Q. 2012, ApJ, 744, 37
Yan, J., Zhang, P., Liu, W., & Liu, Q. 2016, AJ, 151, 104
Yudin, R. V. 2001, A&A, 368, 912
Zamanov, R. K., Stoyanov, K. A., Wolter, U., et al. 2020, MNRAS, 499, 3650
Zhang, S., Qu, J.-L., Song, L.-M., & Torres, D. F. 2005, ApJ, 630, L65

Appendix A: Results of the observations

In this section we present the results of our optical data analysis.

Table A.1. Photometric observations of the optical counterpart to GRO J2058+42.

Date	JD (2,400,000+)	*B*	errB	*V*	errV	*R*	errR	*I*	errI
07-06-2003	52798.507	16.009	0.031	14.913	0.031	14.219	0.027	0.000	0.000
08-06-2003	52799.439	16.067	0.025	14.942	0.021	14.241	0.022	0.000	0.000
24-08-2003	52876.381	16.034	0.020	14.906	0.028	14.259	0.025	13.499	0.034
24-08-2003	52876.381	16.025	0.020	14.894	0.028	14.247	0.025	13.479	0.034
05-07-2004	53192.458	16.029	0.018	14.886	0.014	14.156	0.017	13.350	0.024
27-07-2004	53214.509	16.067	0.024	14.916	0.030	14.193	0.027	13.411	0.041
24-08-2004	53242.434	16.052	0.015	14.956	0.014	14.244	0.012	13.456	0.017
14-09-2004	53263.350	16.041	0.015	14.924	0.016	14.220	0.014	13.468	0.026
01-10-2004	53280.301	16.075	0.017	14.959	0.017	14.238	0.018	13.474	0.019
26-06-2005	53548.515	16.029	0.021	14.924	0.013	14.224	0.018	13.463	0.044
27-07-2005	53579.475	16.071	0.020	14.974	0.013	14.275	0.014	0.000	0.000
20-08-2005	53603.383	16.045	0.020	14.986	0.025	14.282	0.024	0.000	0.000
17-08-2006	53965.390	16.180	0.038	15.060	0.035	14.300	0.051	0.000	0.000
19-08-2006	53967.436	16.095	0.021	14.982	0.029	14.291	0.034	0.000	0.000
25-06-2007	54277.509	16.030	0.020	14.860	0.031	14.080	0.025	0.000	0.029
16-07-2007	54298.476	16.179	0.028	14.845	0.020	14.081	0.020	13.245	0.000
01-09-2007	54345.481	16.030	0.027	14.791	0.021	14.013	0.025	13.187	0.041
02-09-2007	54346.438	16.024	0.028	14.841	0.031	14.042	0.020	13.203	0.021
03-09-2007	54347.562	16.608	0.013	15.138	0.013	14.430	0.017	13.637	0.023
05-08-2008	54684.414	15.982	0.019	14.737	0.020	13.922	0.020	13.062	0.023
29-06-2009	55012.457	15.992	0.025	14.754	0.022	13.943	0.018	13.095	0.018
26-07-2010	55404.420	16.076	0.030	14.893	0.020	14.164	0.025	13.368	0.028
27-07-2010	55405.537	16.080	0.017	14.877	0.011	14.124	0.013	13.305	0.014
02-11-2010	55503.310	16.270	0.019	15.356	0.020	14.432	0.018	13.490	0.021
26-08-2011	55800.369	16.073	0.014	14.874	0.014	14.146	0.015	13.364	0.025
09-09-2011	55814.256	16.048	0.022	14.893	0.023	14.194	0.015	13.433	0.032
29-07-2013	56503.413	16.086	0.019	14.929	0.017	14.243	0.019	13.498	0.022
29-08-2013	56534.3870	16.047	0.023	14.906	0.022	14.193	0.023	13.419	0.039
20-08-2014	56890.4088	16.040	0.021	14.912	0.021	14.206	0.020	13.465	0.027
14-09-2014	56915.3655	16.066	0.022	14.909	0.014	14.183	0.017	13.410	0.027
22-07-2015	57226.4616	16.031	0.020	14.786	0.011	14.009	0.010	13.155	0.012
18-11-2015	57345.2298	15.971	0.015	14.728	0.013	13.934	0.015	13.085	0.015
06-06-2016	57546.4575	15.931	0.017	14.726	0.016	13.897	0.017	13.033	0.029
22-06-2016	57562.5243	15.949	0.019	14.698	0.013	13.890	0.012	13.012	0.029
08-09-2016	57640.2994	16.049	0.090	14.782	0.084	13.970	0.086	13.128	0.093
06-10-2016	57668.2905	15.973	0.011	14.718	0.013	13.883	0.012	12.993	0.013
03-11-2016	57696.3765	15.952	0.018	14.693	0.019	13.861	0.020	13.008	0.024
28-08-2017	57994.3935	15.862	0.020	14.642	0.017	13.835	0.018	12.979	0.025
13-06-2018	58283.4055	15.866	0.051	14.604	0.049	13.736	0.056	12.865	0.070
31-07-2018	58331.4022	15.879	0.021	14.644	0.017	13.813	0.020	13.002	0.033
13-07-2019	58678.3712	15.914	0.027	14.730	0.024	13.915	0.022	13.062	0.036
30-07-2019	58695.3461	15.935	0.014	14.775	0.014	13.964	0.011	13.143	0.019
11-09-2019	58738.3514	15.955	0.017	14.786	0.012	14.014	0.014	13.165	0.022
24-06-2020	59025.4564	16.020	0.016	14.857	0.009	14.107	0.010	13.319	0.013
19-07-2020	59050.3951	15.997	0.013	14.838	0.010	14.094	0.012	13.311	0.021
19-08-2020	59081.3532	16.033	0.012	14.859	0.010	14.128	0.008	13.326	0.013
04-07-2021	59400.3893	16.022	0.017	14.891	0.017	14.184	0.018	13.441	0.022
04-09-2021	59462.3711	16.005	0.024	14.882	0.021	14.174	0.022	13.423	0.031
10-10-2021	59498.3211	16.030	0.036	14.912	0.021	14.231	0.022	13.466	0.026
29-07-2022	59790.3894	16.086	0.013	14.942	0.010	14.271	0.015	13.547	0.025
17-08-2022	59809.3586	16.102	0.014	14.963	0.013	14.267	0.019	13.563	0.020
20-09-2022	59843.3477	16.074	0.015	14.944	0.013	14.271	0.013	13.536	0.019

Table A.2. Polarimetric observations of the optical counterpart to GRO J2058+42.

Date	JD (2,400,000+)	PD (%)	err	EPVA (deg.)	err	q	err	u	err
14-09-2013	56550.4068	4.17	0.26	66.00	1.80	-0.0279	0.0028	0.0310	0.0028
07-10-2013	56573.4279	4.08	0.22	67.56	1.57	-0.0289	0.0027	0.0288	0.0022
25-10-2013	56591.3649	4.09	0.36	66.35	2.54	-0.0277	0.0039	0.0301	0.0036
09-11-2013	56606.2704	4.23	0.24	67.01	1.65	-0.0294	0.0027	0.0304	0.0026
10-05-2014	56787.6089	3.57	0.63	60.58	5.19	-0.0185	0.0077	0.0305	0.0057
08-07-2014	56846.5993	3.18	0.42	69.20	3.85	-0.0238	0.0042	0.0211	0.0044
01-08-2014	56870.5431	3.94	0.27	62.08	1.99	-0.0221	0.0028	0.0326	0.0029
14-08-2014	56883.5078	4.38	0.25	68.54	1.66	-0.0321	0.0028	0.0299	0.0027
11-06-2015	57184.5220	4.58	0.13	67.50	0.84	-0.0324	0.0018	0.0324	0.0018
06-08-2015	57240.5489	4.42	0.12	66.89	0.81	-0.0306	0.0018	0.0319	0.0016
15-06-2016	57554.5689	4.45	0.17	67.78	1.09	-0.0318	0.0021	0.0312	0.0019
09-09-2016	57641.4888	4.82	0.13	66.95	0.77	-0.0334	0.0018	0.0347	0.0018
03-10-2016	57665.2876	4.79	0.13	66.89	0.76	-0.0331	0.0018	0.0346	0.0017
02-11-2016	57695.2729	4.49	0.12	66.65	0.73	-0.0308	0.0016	0.0327	0.0016
24-06-2017	57929.4772	4.76	0.13	68.82	0.80	-0.0352	0.0018	0.0321	0.0017
10-07-2017	57945.4809	4.61	0.13	65.87	0.79	-0.0307	0.0018	0.0344	0.0016
31-07-2017	57965.5018	4.45	0.16	67.65	1.03	-0.0316	0.0022	0.0313	0.0016
17-10-2017	58044.2878	4.39	0.12	66.42	0.81	-0.0298	0.0017	0.0322	0.0016
29-06-2018	58298.5334	4.78	0.15	66.71	0.91	-0.0328	0.0021	0.0347	0.0018
01-09-2018	58363.3993	4.66	0.14	65.62	0.84	-0.0307	0.0020	0.0350	0.0016
24-09-2018	58386.4209	4.62	0.15	65.35	0.92	-0.0301	0.0021	0.0350	0.0017
27-10-2018	58419.2449	4.89	0.16	65.64	0.94	-0.0322	0.0022	0.0367	0.0018
03-11-2018	58426.2604	4.76	0.16	66.51	0.93	-0.0325	0.0021	0.0348	0.0018
17-06-2019	58652.4635	4.78	0.14	64.43	0.86	-0.0300	0.0020	0.0372	0.0018
14-07-2019	58679.4369	4.95	0.13	65.65	0.74	-0.0327	0.0018	0.0372	0.0018
24-08-2019	58720.4205	4.90	0.14	67.29	0.82	-0.0344	0.0019	0.0349	0.0018
27-08-2019	58723.3256	5.18	0.14	65.23	0.80	-0.0336	0.0020	0.0394	0.0019
16-09-2019	58743.3588	4.91	0.15	65.06	0.85	-0.0317	0.0020	0.0376	0.0018
19-06-2020	59019.5386	5.05	0.13	66.07	0.73	-0.0339	0.0019	0.0374	0.0018
01-07-2020	59031.5139	5.08	0.13	65.70	0.74	-0.0336	0.0019	0.0381	0.0018
14-08-2020	59076.2758	4.98	0.15	65.99	0.88	-0.0333	0.0020	0.0370	0.0019
18-06-2021	59383.5611	5.00	0.26	66.39	1.48	-0.0340	0.0026	0.0367	0.0031
27-07-2021	59423.4226	4.85	0.21	65.94	1.23	-0.0324	0.0027	0.0361	0.0021
16-08-2021	59443.3635	4.65	0.20	65.83	1.24	-0.0309	0.0026	0.0348	0.0020
25-08-2021	59452.3016	4.97	0.20	65.08	1.15	-0.0320	0.0027	0.0379	0.0021
27-09-2021	59485.4348	5.24	0.21	64.58	1.13	-0.0331	0.0028	0.0406	0.0022
07-10-2021	59495.3763	4.75	0.21	64.63	1.24	-0.0300	0.0027	0.0367	0.0021
15-07-2022	59776.4256	4.12	0.11	66.63	0.76	-0.0282	0.0015	0.0300	0.0015

Table A.3. Polarimetric observations of selected field stars in the field of view of GRO J2058+42.

ID	JD (2,400,000+)	PD (%)	EPVA (deg.)	q	u
fs1	56883.512	3.98 ± 0.15	68.3 ± 1.1	−0.0289 ± 0.0018	0.0273 ± 0.0018
fs2	57665.300	0.87 ± 0.13	49.6 ± 4.4	−0.0014 ± 0.0014	0.0085 ± 0.0013
gfs2	59496.319	5.38 ± 0.45	63.6 ± 2.3	−0.0326 ± 0.0047	0.0428 ± 0.0048

Table A.4. Results of the spectral analysis. Observations marked with a † correspond to single-peak profiles.

Date	JD (2,400,000+)	EW(Hα) (Å)	Err_EW (Å)	ΔV (km s^{-1})	Err_ΔV (km s^{-1})	log(V/R)	Err_log(V/R)	Telescope
2004-06-25	53182	3.86	0.30	417	15	-0.074	0.057	SKO
2004-07-06	53193	4.85	0.34	425	19	-0.036	0.046	SKO
2004-08-25	53243	4.16	0.23	398	13	-0.067	0.036	SKO
2004-09-13	53262	4.91	0.19	392	9	-0.019	0.030	SKO
2004-10-03	53282	4.49	0.27	378	15	-0.046	0.044	SKO
2004-10-24	53303	2.93	0.25	431	20	-0.034	0.056	SKO
2005-06-22	53544	0.27	0.16	627	32	-0.099	0.153	SKO
2005-07-12	53564	0.48	0.10	557	18	-0.036	0.126	SKO
2005-07-13	53565	0.31	0.11	609	20	0.178	0.128	SKO
2005-07-29	53581	1.19	0.13	572	14	0.042	0.076	SKO
2005-08-16	53599	0.87	0.09	592	20	-0.207	0.107	SKO
2005-09-20	53634	1.36	0.14	529	20	0.029	0.087	SKO
2005-10-26	53670	1.77	0.33	527	15	-0.075	0.079	SKO
2006-06-20	53907	2.48	0.17	458	20	-0.038	0.110	SKO
2006-10-02	54011	3.21	0.41	499	18	0.002	0.070	SKO
2006-10-24	54033	2.66	0.15	506	14	-0.113	0.055	SKO
2007-05-14	54235	3.57	0.24	374	70	-0.076	0.106	SKO
2007-05-29	54250	4.31	0.21	393	15	-0.069	0.056	SKO
2007-09-05	54349	5.70	0.19	352	10	0.030	0.026	SKO
2007-09-11	54355	6.17	0.15	355	10	-0.003	0.026	SKO
2007-10-02	54376	5.03	0.19	370	16	-0.072	0.040	SKO
2007-10-03	54377	5.07	0.17	365	11	-0.111	0.035	SKO
2007-10-04	54378	5.13	0.11	386	10	-0.097	0.029	SKO
2008-06-24	54642	7.35	0.21	345	10	-0.095	0.022	SKO
2008-06-26	54644	7.28	0.16	326	12	-0.138	0.028	SKO
2008-07-15	54663	7.14	0.20	374	27	-0.139	0.052	SKO
2008-08-12	54691	7.00	0.18	325	15	-0.140	0.034	SKO
2008-09-02	54712	7.46	0.18	323	16	-0.041	0.037	SKO
2009-07-29	55042	9.37	0.16	317	8	-0.015	0.019	SKO
2009-08-11	55055	8.61	1.00	333	19	0.033	0.051	SKO
2009-09-28	55103	10.02	0.25	322	14	-0.043	0.030	SKO
2010-08-02	55411	7.67	0.15	351	7	0.047	0.021	SKO
2010-08-27	55436	7.51	0.17	333	8	-0.008	0.020	SKO
2010-09-14	55454	8.43	0.16	359	8	0.031	0.019	SKO
2010-09-30	55470	8.47	0.16	316	10	-0.021	0.025	SKO
2010-11-03	55504	7.24	0.30	360	24	-0.181	0.064	SKO
2011-04-09	55661	7.46	0.64	302	17	0.051	0.058	LT
2011-04-23	55675	7.84	0.67	332	19	0.031	0.049	LT
2011-05-15	55697	6.22	0.31	293	18	-0.029	0.127	LT
2011-05-20	55702	6.89	0.51	327	20	0.073	0.054	LT
2011-06-12	55725	6.47	0.37	308	51	-0.074	0.118	LT
2011-06-17	55730	7.61	0.38	356	14	-0.029	0.041	LT
2011-06-25	55738	7.21	0.22	339	10	0.018	0.040	LT
2011-07-02	55745	7.97	0.34	336	18	0.016	0.056	LT
2011-07-08	55751	7.25	0.43	356	14	-0.119	0.038	LT
2011-07-15	55758	6.62	0.38	388	19	0.087	0.056	LT
2011-08-03	55777	7.50	0.20	368	7	0.012	0.021	SKO
2011-10-07	55842	6.42	0.48	353	13	-0.028	0.054	LT
2011-10-14†	55849	4.29	0.37	–	–	–	–	LT
2011-12-02	55898	5.20	0.32	362	16	0.015	0.066	LT
2012-03-11	55998	3.44	0.68	454	33	0.058	0.063	LT
2012-06-06	56085	3.85	0.18	420	8	0.014	0.030	SKO
2012-08-24	56164	1.71	0.07	493	14	-0.100	0.073	SKO
2012-08-25	56165	2.26	0.23	503	16	-0.188	0.098	SKO
2012-09-02	56173	1.16	0.25	485	18	-0.111	0.109	LT

Table A.4. continued.

Date	JD (2,400,000+)	EW(Hα) (Å)	Err_EW (Å)	ΔV (km s^{-1})	Err_ΔV (km s^{-1})	log(V/R)	Err_log(V/R)	Telescope
2012-09-06	56177	2.21	0.26	485	13	-0.015	0.070	SKO
2012-09-29	56200	1.26	0.26	578	31	-0.138	0.125	LT
2012-10-19	56220	1.67	0.15	548	14	0.011	0.068	SKO
2012-10-26	56227	1.68	0.38	570	43	-0.109	0.145	LT
2013-05-17	56430	2.74	0.53	427	34	0.092	0.148	LT
2013-06-21	56465	2.98	0.49	451	37	0.101	0.118	LT
2013-06-28	56472	1.99	0.23	464	25	0.190	0.102	LT
2013-07-19	56493	2.38	0.23	506	18	-0.013	0.090	LT
2013-07-26	56500	3.53	0.27	459	16	0.004	0.063	LT
2013-07-30	56504	3.18	0.17	452	9	-0.025	0.042	SKO
2013-08-30	56535	3.35	0.20	475	10	0.014	0.035	SKO
2013-10-18	56584	2.65	0.11	448	8	0.023	0.042	SKO
2014-06-06	56815	4.56	0.15	395	16	0.073	0.050	SKO
2014-08-05	56875	2.34	0.14	472	11	0.020	0.048	SKO
2014-08-19	56889	2.28	0.15	500	11	-0.061	0.052	SKO
2014-10-12	56943	2.33	0.14	496	10	-0.020	0.052	SKO
2015-06-23	57197	4.29	0.21	374	10	0.058	0.031	SKO
2015-07-08	57212	4.54	0.24	347	9	0.038	0.027	SKO
2015-07-21	57225	5.01	0.23	355	22	0.002	0.056	SKO
2015-10-05	57301	5.22	0.22	346	12	0.050	0.040	SKO
2015-11-27	57354	5.52	0.21	353	18	0.050	0.053	LT
2016-04-23	57502	7.14	0.21	310	17	0.042	0.042	LT
2016-04-28	57507	7.73	0.34	307	11	-0.042	0.029	LT
2016-05-15	57524	7.84	0.37	240	29	0.086	0.085	LT
2016-05-21	57530	7.48	0.25	287	28	9.999	0.000	LT
2016-06-08	57548	6.89	0.10	273	78	-0.056	0.207	SKO
2016-07-12	57582	7.66	0.26	307	15	-0.047	0.037	LT
2016-07-18	57588	7.52	0.29	316	19	0.005	0.043	LT
2016-09-06	57638	6.79	0.15	405	38	-0.080	0.066	SKO
2016-09-14	57646	7.97	0.30	272	11	0.001	0.000	LT
2016-10-04	57666	6.52	0.13	333	11	0.129	0.026	SKO
2016-10-14	57676	7.49	0.20	306	13	-0.045	0.033	LT
2017-05-16	57890	8.10	0.90	398	54	-0.077	0.088	LT
2017-05-28	57902	8.04	0.83	303	15	0.040	0.038	LT
2017-06-03	57908	7.54	0.84	269	45	-0.010	0.115	LT
2017-06-08	57913	9.45	0.58	262	46	0.130	0.126	LT
2017-06-13	57918	8.24	0.76	248	27	0.048	0.074	LT
2017-06-21	57926	10.24	0.92	264	17	-0.228	0.044	LT
2017-06-26	57931	8.17	0.84	242	20	0.077	0.060	SKO
2017-06-29	57934	9.09	0.38	268	23	-0.177	0.062	LT
2017-07-13	57948	8.23	0.20	324	8	-0.040	0.019	SKO
2017-08-13	57979	8.33	0.32	295	27	-0.060	0.063	LT
2017-09-02	57999	8.10	0.17	270	26	-0.127	0.066	LT
2017-09-17	58014	8.20	0.32	286	17	-0.034	0.043	LT

Table A.4. continued.

Date	JD (2,400,000+)	EW(Hα) (Å)	Err_EW (Å)	ΔV (km s^{-1})	Err_ΔV (km s^{-1})	log(V/R)	Err_log(V/R)	Telescope
2017-09-29	58026	7.72	0.24	339	15	0.047	0.041	LT
2017-10-13	58040	8.77	0.18	281	12	0.065	0.028	SKO
2018-04-05	58214	9.03	0.31	296	27	0.054	0.066	LT
2018-04-29†	58238	7.94	0.35	–	–	–	–	LT
2018-05-27	58266	10.10	0.31	292	24	-0.176	0.065	LT
2018-06-06	58276	10.36	0.18	268	25	0.073	0.059	LT
2018-08-18†	58349	9.74	0.19	–	–	–	–	LT
2018-08-23	58354	9.05	0.16	256	12	-0.045	0.033	SKO
2018-08-25	58356	8.30	0.17	282	10	0.048	0.026	SKO
2018-08-29	58360	8.96	0.20	274	27	0.019	0.064	LT
2018-09-09	58371	8.82	0.23	288	21	0.057	0.050	LT
2018-09-18	58380	8.46	0.14	309	9	-0.063	0.021	SKO
2018-09-21	58383	9.00	0.25	282	31	-0.255	0.096	LT
2018-10-08	58400	8.78	0.16	276	10	-0.032	0.025	SKO
2019-04-17	58591	11.20	0.30	329	24	0.022	0.051	
2019-04-27	58601	11.35	0.43	296	29	0.066	0.070	LT
2019-05-08†	58612	12.40	0.31	–	–	–	–	LT
2019-05-19	58623	11.82	0.24	278	27	-0.215	0.077	LT
2019-05-29	58633	10.90	0.24	322	15	-0.159	0.039	LT
2019-06-13	58648	12.97	0.34	330	21	-0.041	0.044	LT
2019-06-23	58658	12.71	0.37	360	14	-0.003	0.037	LT
2019-07-19	58684	13.02	0.33	294	18	0.015	0.040	LT
2019-07-29	58694	13.58	0.27	293	7	0.004	0.017	SKO
2019-08-10	58706	13.82	0.47	289	24	-0.107	0.060	LT
2019-08-19	58715	13.01	0.28	286	12	-0.197	0.032	SKO
2019-09-09	58736	12.23	0.18	331	7	-0.035	0.016	SKO
2019-09-24	58751	11.99	0.22	327	7	-0.020	0.017	SKO
2019-10-09	58766	13.11	0.40	326	8	-0.001	0.021	LT
2020-06-22	59023	9.12	0.26	350	6	0.029	0.015	SKO
2020-07-20	59051	9.66	0.21	333	5	-0.049	0.014	SKO
2020-08-05	59067	7.62	0.13	326	70	0.045	0.126	LT
2020-08-25	59087	8.54	0.21	340	8	-0.050	0.022	SKO
2020-09-14	59107	8.63	0.23	330	7	-0.037	0.018	SKO
2020-09-16	59109	8.72	0.29	371	30	-0.094	0.066	SKO
2020-09-29	59122	8.65	0.23	322	10	0.006	0.023	SKO
2020-09-30	59123	8.27	0.49	336	14	-0.077	0.057	LT
2020-10-30	59153	8.74	0.35	346	14	-0.027	0.050	LT
2021-07-02	59398	6.96	0.20	388	6	-0.052	0.017	SKO
2021-08-11	59438	6.43	0.28	348	7	-0.130	0.022	SKO
2021-09-01	59459	6.35	0.19	370	4	-0.005	0.017	SKO
2021-09-05	59463	6.65	0.25	377	5	-0.008	0.019	SKO
2021-09-29	59487	6.59	0.20	377	6	-0.056	0.020	SKO
2022-05-24	59724	3.26	0.29	420	9	0.065	0.035	SKO
2022-06-15	59746	2.72	0.20	442	8	-0.021	0.039	SKO
2022-07-04	59765	3.26	0.10	442	8	-0.144	0.037	SKO
2022-07-06	59767	2.82	0.18	415	11	0.005	0.045	SKO
2022-07-30	59791	1.35	0.17	502	12	0.032	0.061	SKO
2022-09-08	59831	1.15	0.12	532	11	0.158	0.057	SKO
2022-09-09	59832	1.75	0.21	530	11	0.058	0.053	SKO
2022-09-19	59842	1.52	0.12	505	9	-0.004	0.047	SKO